applied optics

Multichannel laser diode to polymer waveguide array coupling with a double-aspheric lens

K. Kunze,[1,*] C. Gossler,[1,2] M. Reinhardt,[1,3] M. Arnold,[4] F. Schwenzer,[4] C. Helke,[3,4]
D. Reuter,[3,4] D. Keppeler,[2] T. Moser,[2] and U. T. Schwarz[1]

[1]*Technical University of Chemnitz, Experimental Sensor Science, Reichenhainer Str. 70, 09126 Chemnitz, Germany*
[2]*University Medical Center of Goettingen, Institute for Auditory Neuroscience, Robert-Koch-Str. 40, 37075 Goettingen, Germany*
[3]*Fraunhofer Institute for Electronic Nano Systems ENAS, Technologie-Campus 3, 09126 Chemnitz, Germany*
[4]*Technical University of Chemnitz, Center for Microtechnologies (ZfM), Reichenhainer Str. 70, 09126 Chemnitz, Germany*
*katharina.kunze@physik.tu-chemnitz.de

An optical system for multichannel coupling of laser arrays to polymer waveguide array probes with a single biconvex lens is developed. The developed cylindrical module with 13 mm and 20 mm in diameter and length, respectively, enables coupling of eight individual optical channels using an aspheric lens. Specific coupling with crosstalk below −13 dB for each channel and quasi-uniform coupling over all channels is achieved for a waveguide array with 100 μm lateral facet pitch at the incoupling site. The polymer waveguide technology allows for tapering of the lateral waveguide pitch to 25 μm toward the tip of the flexible waveguide array. SU-8 and PMMA are used as the waveguide core and cladding, respectively. The optical coupling module is designed as a prototype for preclinical evaluation of optical neural stimulators. © 2023 Optica Publishing Group

1. INTRODUCTION

This multichannel coupling system is part of the development of a preclinical optical cochlear implant (oCI) [1,2], but it can be generalized also to other biomedical stimulators such as for the brain. The oCI aims to overcome limitations of the well-established electrical cochlear implant (eCI), a medical device used to artificially restore hearing in patients suffering from profound hearing loss or deafness. An eCI uses an array of electrodes implanted into the cochlea to stimulate the spiral ganglion neurons forming the auditory nerve. The tonotopic organization of the cochlea enables the matching of the different electrode positions to a respective range of audible frequencies, but extensive current spreading around these electrodes limits the spatial resolution of the artificial sound encoding system due to the conductive extracellular fluids of the cochlea chambers. Instead, the oCI uses light for optogenetic stimulation of the spiral ganglion neurons, which promises increased spatial resolution and therefore improved hearing quality since light can be better confined in its spatial propagation [3]. Implementations considered thus far include insertable arrays of μLED- or laser-based and waveguide-based optical stimulators [2]. In the latter, a waveguide array is used to guide laser light from a laser array, placed in a sealed housing outside the cochlea, to different tonotopic positions within the cochlea, more precisely to the spiral ganglion neurons. This requires a waveguide structure with an incoupling structure that allows for efficient laser-to-waveguide coupling over tens to hundreds of channels, and an

outcoupling structure that fits the intracochlear space in size and mechanical properties, e.g., flexibility to bend along the spiral cochlea. Given a mean diameter of the scala tympani of smaller than 300 μm for mice, used for preclinical tests, and 900 μm for humans [4], size is a crucial factor. It has been shown that bundles of up to eight commercially available glass fibers can be inserted into a human cochlea [5], but for more fibers the total bundle size and bending radius exceed the requirements. Polymer-based waveguides, on the other hand, offer an approach for arrays with an increased number of optical channels and better mechanical conformity [2].

Waveguides are fundamental for optogenetic research and applications. They are widely used for optical stimulation of activity in neural tissue but also for imaging the respective tissue. Thus, there are various designs to meet the particular requirements. For endoscopic imaging, fiber bundles connected to lenses allow for small diameter designs with comparably high numerical aperture (NA) [6,7]. Thus, they can be used in small structures with low-light conditions. Adding aspherical or gradient-index (GRIN) lenses to the fiber bundle solves the issue of limited light-gathering ability due to a low NA, but chromatic aberrations have severe impact on the image quality [8]. Structures for stimulation range from single waveguides [9] for targeting specific positions to waveguide arrays, which can deliver light to certain areas [10,11], or even targets in a three-dimensional pattern within the nervous system [12], accessing not only the surface but also deep brain regions. Since the light

for stimulation purposes is typically monochromatic, chromatic aberrations do not present an issue in contrast to imaging applications. Yet the coupling efficiency between the light source and waveguide remains an important factor, especially concerning the energy management in portable or implantable, untethered devices.

Laser light can be coupled into waveguides in several ways, ranging from butt coupling [13] and single spherical lenses [14] to multi-lens systems [15], mainly varying in coupling efficiency and system complexity. The achievable coupling efficiency is higher for lens coupling compared to butt coupling, but it is also more susceptible to misalignment and aberrations [16–18]. The coupling system for optogenetic stimulators requires a certain working distance between the laser and waveguide array since the optical components must be separated by a sapphire window, which serve as the optical window within the hermetically sealed housing that is typically made of titanium [19]. The sapphire window is necessary to pass the light, generated by the laser diodes inside the housing, to the waveguides outside the housing. To bridge that distance, a lens coupling system is a possible approach. However, common optical coupling systems based on lens-couplers use ball lenses [20], which produce low coupling efficiencies to waveguide arrays due to spherical aberration, or lensed-fiber designs [21,22], that do not achieve the necessary working distances. Coupling systems specifically designed for optogenetic applications also make use of GRIN lenses [23], but have too small working distances, and spherical microlenses [24], which can achieve the necessary working distances, but their diameters do not match our intended lateral pitch of 100 µm.

The developed system is designed to work with only one aspheric lens for coupling the output of a linear array of edge-emitting lasers into a waveguide array. Using a single lens for all channels comes with the advantage of comparably little occupied space but also at the expense of decreasing coupling efficiency for off-axis optical beams due to aberrations that influence the focus size adversely and usually can be corrected by additional lenses. Focusing the laser beams to small waist diameters is well manageable for a laser perfectly aligned with the optical axis, but it can get difficult for an increasing lateral laser offset. Furthermore, the possible number of channels is not only limited by the field of view but also the field curvature,

which can make coupling for an array, even with well focused beams, challenging.

In earlier studies (not discussed), we investigated several lenses and lens systems, such as ball lenses, GRIN lenses, a microlens objective (for endoscopic imaging), and lens pairs (for laser to fiber coupling). Neither achieved the wide and flat field of view necessary for this specific application combined with the high NA required for laser diode coupling, which resulted in inefficient and non-uniform coupling.

2. LENS COUPLING

This system is based on coupling each laser within the array to a specific waveguide by focusing the divergent and asymmetric laser beams through a single aspheric biconvex lens and placing the waveguide facets at the focal points for coupling. As shown in Fig. 1, the lasers are arranged in a linear array along the slow axis, symmetrically to both sides of the optical axis of the lens. The same configuration applies for the waveguide array.

The single lens approach comes with challenges regarding various aberrations, mainly astigmatism and field curvature. Astigmatic behavior, due to asymmetric transmission of a beam through a lens, is a result of the circumstance that the lasers in this system are placed with an offset to the optical axis of the lens, and additionally the astigmatic nature of the laser diode beam [25]. Here, the more critical aberration is the field curvature, which is due to the placement of the lasers within the array in various distances to the optical axis. The waveguide facets are arranged in a plane perpendicular to the optical axis. Thus, foci appearing out of this certain plane due to field curvature aberration may suffer significant decrease in coupling efficiency. The limits of this system are highly dependent on the extent, to which those two aberrations occur for the specific lens in use. Aspheric lenses reduce different aberrations, first of all spherical aberration, and therefore were chosen for this application. They can replace systems made of several spherical lenses with similar performance and thus enable smaller and cost-effective systems [26].

3. DESIGN OF THE COUPLING MODULE

The coupling module mounts and aligns the components for eight channel coupling along the optical axis. Figure 2 shows a
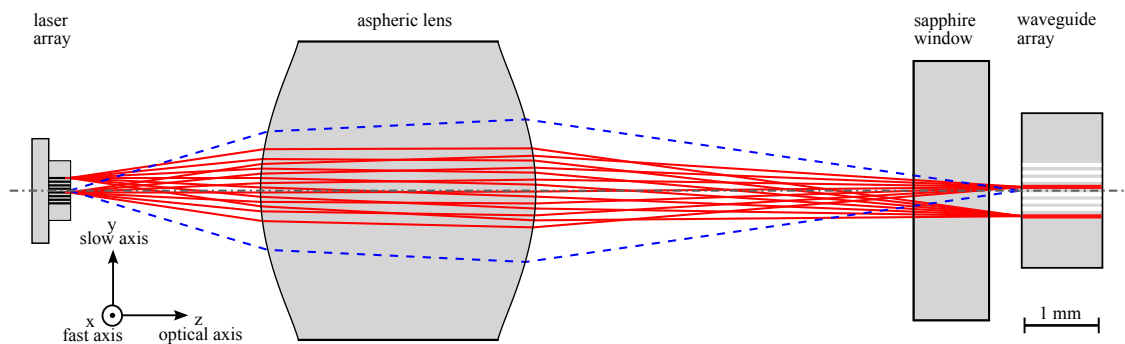
Fig. 1. Schematic of the multibeam laser diode-to-waveguide array coupling system; the red lines represent the slow axis expansion angle (16.9°, full angle) of the Gaussian beams ($1/e^2$) for two channels, the blue dashed lines outline the fast axis Gaussian beam expansion angle (33.3°, full angle) in the perpendicular plane; the latter is plotted for the central channel but is similar for all channels.
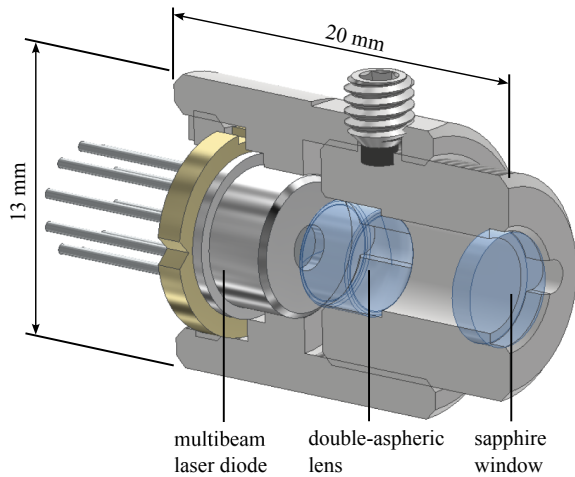
Fig. 2. Sectional view of the coupling module; the multibeam laser diode, double-aspheric lens, and sapphire window are aligned to the optical axis.

schematic of this module, containing laser diode array, lens, and sapphire window.

A. Multibeam Laser Diode

The laser array is a multibeam laser diode HL67aasBH (Ushio, Japan) that consists of eight semiconductor lasers at a 50 μm pitch on a single chip, housed in a standard TO-9 package. The diode chip is connected to a printed circuit board (PCB) to control the status of all individual emitters.

B. Double-Aspheric Lens

A biconvex/double-aspheric lens "355440" (LightPath Technologies, Orlando, FL, USA) with two identical surfaces and an antireflection coating is used for this module. Its design and surface parameters are listed in Appendix A. It is specifically designed for laser-to-fiber coupling with a single lens. A lateral magnification $\beta = 2$ is important for handling the different pitch values for laser and waveguide arrays of 50 μm and 100 μm, respectively. Due to this specific magnification, the NA is halved for coupling into the waveguide in respect to the laser NA, a fact that can increase the coupling efficiency, because

the light has to hit the waveguide facet in an angle within the waveguide's acceptance cone. Thus, a smaller beam NA in comparison to the waveguide NA supports higher coupling efficiency. It also results in a focus diameter double the size of the laser facet, which may lead to decreasing coupling efficiencies, in contrast.

C. Polymer Waveguide Array

The design and fabrication of the waveguide arrays is described in detail in Helke *et al.* In brief, the waveguide array, as shown in Fig. 3, includes 10 waveguides with a lateral pitch of 100 μm at the incoupling facet, of which the inner eight were used for coupling. Each waveguide has a rectangular facet with 5 μm in height (fast axis) and 20 μm in width (slow axis), and then it narrows to a smaller size of $5 \times 10 \ \mu m^2$ and ends in an outcoupling structure, which scatters the light away from the longitudinal array axis. The array has an expanded side for coupling. From there, the waveguide structure narrows to the tapered side, where the waveguides end in their respective outcoupling structures that are arranged with 250 μm and 25 μm longitudinal and lateral distance, respectively, to each other. This design is necessary for enabling specific coupling at the coupling site and meeting the scale of the cochlea of the animal model (here: Mongolian gerbils) toward the outcoupling structure for implantation. Also, the NA of the waveguide is about 0.56 and thus exceeds the lenses NA of 0.3, which is necessary to ensure total internal reflection after coupling.

The polymer waveguide technology uses microsystem technology on 150 mm silicon wafers as temporary carriers within a reproduceable waver-level fabrication process. Main microsystem technology processes are lithography (e.g., for spin coating of different polymer layers, exposure, and development of the waveguide structures), deposition (e.g., of hardmasks), etching (e.g., for structuring the waveguide structures) to define 5-μm-high SU-8 waveguides, the surrounding PMMA cladding layers, and the sacrificial layer LOR 10B. The probes are separated using a scribe and break process for the silicon wafer. The incoupling waveguide core facets are defined during the scribe and break process. Afterward the probes are partially released from the temporary silicon substrate wafer by removing the LOR 10B sacrificial layer with an alkaline developer. The region beneath the incoupling facets remains on the silicon substrate to
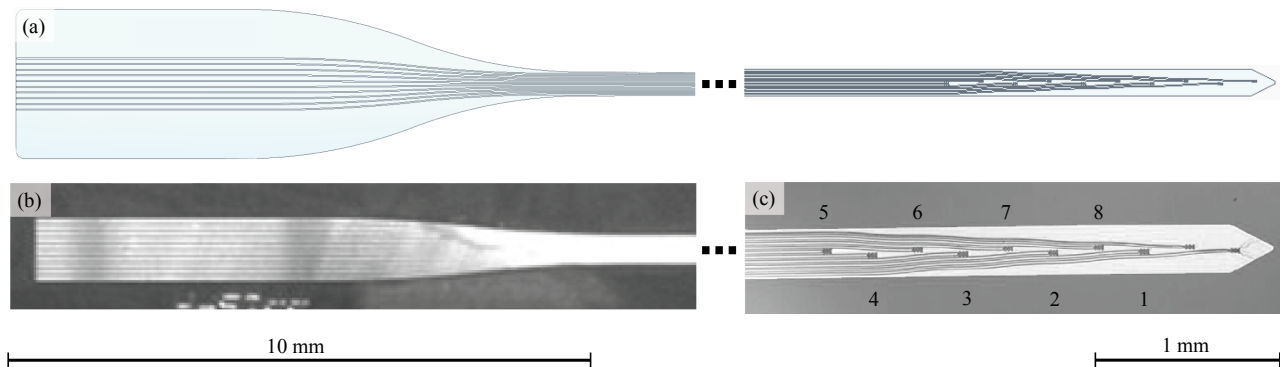
Fig. 3. (a) Waveguide array (schematic), including 10 waveguides with (b) coupling facets (lateral pitch 100 μm) and (c) their respective outcoupling structures (longitudinal distance 250 μm, lateral pitch 25 μm); the two outmost waveguides, with their respective outcoupling structures closest to the tip, will not be used for coupling; the numbering order of the outcoupling structures results from the order of the coupling facets.

facilitate handling and ensure a precise pitch of the waveguide facets [27].

D. Module

The laser diode is mounted in a metal tube. A second tube contains the lens and a sapphire window with 1 mm thickness. Laser and lens tubes are screwed together with a fine thread (pitch 0.5 mm) and adjusted to the working distance from laser to lens (2.63 mm for laser wavelength $\lambda = 650$ nm), where the foci have a lateral pitch of 100 µm. The third section includes the mounted waveguide array, which is placed behind the sapphire window, adjusted to the position for uniform coupling over all channels using a 5-axis stage. The waveguide module is to be bonded to the sapphire window with a transparent epoxy seal that fills the gap between the window and waveguide array.

The lens is 4.7 mm in diameter and the distance from the laser array (emitters) to the waveguide array (facets) is 13.7 mm. These measures define the minimal size of the coupling system, assuming that the epoxy seal is filling a gap of 0.9 mm between sapphire window and waveguide array and using a laser array package with a 0.25 mm thick optical window. The full module size exhibits a 13 mm lateral diameter and 20 mm length along the optical axis, as shown in Fig. 4, not taking into account the waveguide array.

The diameter of the lens does allow integration into the planned hermetically sealed oCI housing with a thickness of about 6 mm. The optical design would also allow the reduction of the lens diameter to about 4 mm without increasing losses dramatically (see Fig. 1). Here, we investigate the optical properties and coupling efficiencies and are therefore not strictly bound by the geometrical constriction of a human oCI. The compact size of the current design still allows for preclinical investigations.

4. EXPERIMENTS AND DISCUSSION
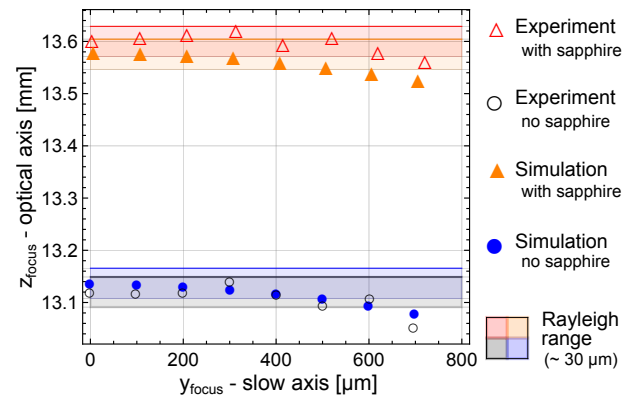
A. Focus Position

Figure 5 shows the schematic representation of the setup used to evaluate the focal point shift in relation to laser offset within the array. A multibeam laser diode, with a removed can for closer access, is mounted on a 3-axis stage. For each laser emitter position, a series of pictures of the beam profile at several equidistant
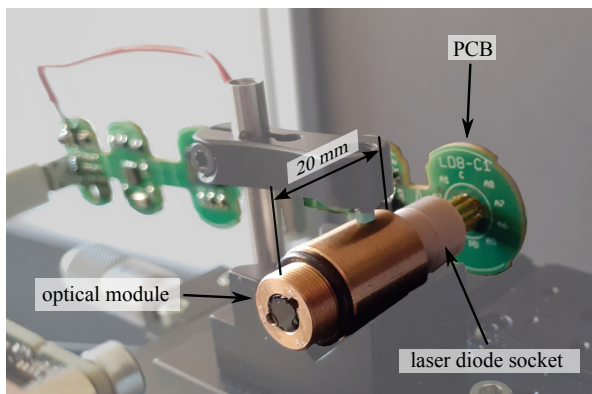
Fig. 4. Coupling module (without waveguide array) connected to a laser driver PCB.
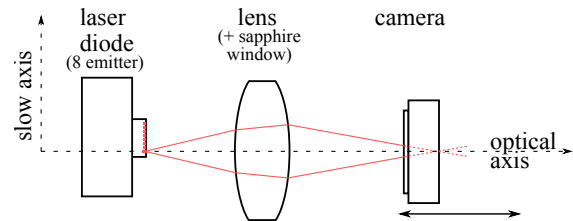
Fig. 5. Schematic of setup for focus measurement.

Fig. 6. Focus positions resulting from laser positions with 0 to 350 µm lateral distance (step size 50 µm) to the optical axis. The lens lateral magnification ($\beta = 2$) results in focus distances to the optical axis (y_{focus}) with a step size of about 100 µm. Simulated and measured values for a system with and without sapphire window with working distances (laser to lens) WD = 2.63 mm.

positions along the optical axis is taken, using a CMOS camera with 2.2 µm pixel size. The pictures are then evaluated relative to the standard deviation of the pixel brightness values in respect of their spatial distribution. The picture showing the smallest standard deviation is expected to represent the focus for the respective laser position and provides information about focus size and position. The experiment is done with and without the sapphire window.

Figure 6 shows the measured and simulated focus positions along the optical and slow axis. The simulation method is detailed in Appendix B. We derive that measured focus positions agree well with simulated values for the system without the sapphire window, with differences between the measured and calculated positions of 7.4 ± 14.81 µm (mean ± SD) in the direction of the optical axis and 0.15 ± 1.56 µm for the slow axis. The exact lateral focus values are also displayed in Table 1 and demonstrate that there is about 100 µm pitch (at 50 µm laser pitch), which is in agreement with the lens lateral magnification. The system with the sapphire window comes with higher differences of 40.3 ± 11.0 µm and 9.1 ± 6.9 µm for the optical and slow axis, respectively.

Because the lasers are positioned along the slow (y) axis directly in the y-z plane, the respective foci should have no offset to this plane. For the simulation, all focus positions occur exactly in that plane. The measured positions, with and without sapphire window, have a y axis offset of less than 0.4 µm.

The plotted positions in Fig. 6 also show the field curvature, which results in a decreasing coupling efficiency displayed in

Table 1.   Focus Positions on the Slow Axis[a]

| | Focus Position y_{focus} [μm] | | | |
| | No Sapphire | | With Sapphire | |
Laser Position y_{laser} [μm]	Simulation	Measurement	Simulation	Measurement
0	0	0	0	0
50	101.0	99.0	100.9	103.4
100	201.5	200.2	201.6	204.6
150	301.9	301.4	302.0	310.2
200	401.7	402.6	401.9	411.4
250	501.1	501.6	501.3	517.0
300	599.9	602.8	600.3	616.0
350	698.9	697.4	699.1	717.2

[a]As displayed in Fig. 6, depending on the respective laser position at a working distance WD = 2.63 mm ($\beta = 2$); for systems with and without a sapphire window.
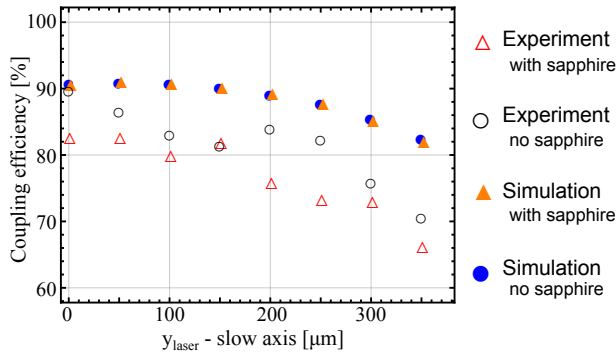

Fig. 7.   Coupling efficiencies for laser positions y_{laser} with 0 to 350 μm distance (step size 50 μm) to the optical axis for waveguide facets with size $19.8 \times 6.6 \,\mu m^2$ ($= 9 \times 3$ pixel); simulated and measured values for a system with and without sapphire window.

Fig. 7. The measured coupling efficiency value is calculated as the ratio of the summed up pixel brightness values within a certain area (9×3 pixel $= 19.8 \times 6.6 \,\mu m^2$), representing the waveguide facet, to the total of all brightness values within the picture. Thus, effects of reflection loss on the lens and waveguide surfaces are not taken into account, and ideal, loss-free coupling into the waveguide is assumed. This also applies for the simulated efficiency as reflection is not implemented in the simulation. For laser positions with up to 200 μm lateral offset of the optical axis, the efficiency remains nearly constant, as well as the focus positions along the optical axis, varying only within the Rayleigh range of about 30 μm for the laser beams fast axis. Thus, within this certain range of laser positions on both sides of the optical axis, a uniform coupling efficiency over all channels can be provided. With a 50 μm pitch, this range spans 9 channels.

B. Scattered Light Measurement

Stray light at the waveguide outcoupling structure is measured using the optical coupling module, with the waveguide array section mounted on a 5-axis stage (3 translation axes, 2 rotation axes). The waveguide array is aligned to the coupling module so that coupling is possible for all eight channels concurrently. The measurement is then executed for each channel activated individually. The result for a single channel is shown in Fig. 8.
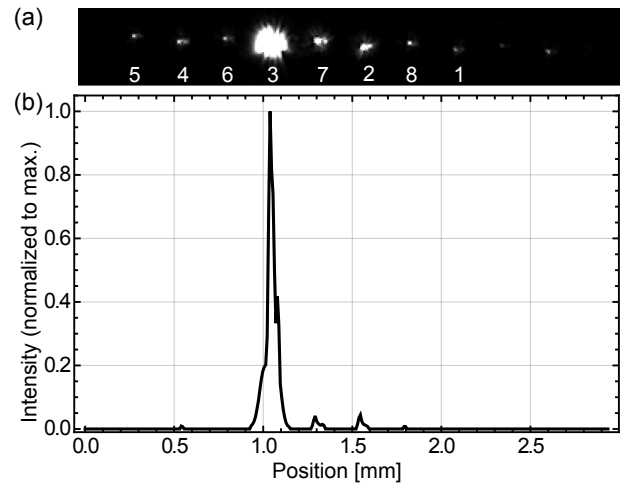
Fig. 8.   (a) Outcoupling structure of the waveguide array with a single laser turned on, numbering according to Fig. 3; (b) intensity profile of the shown outcoupling structure.

The main peak at the indicated outcoupling structure clearly suggests that most of the laser light is coupled into the active channel waveguide and only a small fraction ends up in the surrounding waveguides and cladding, which validates the system's ability of coupling into a specific waveguide. It is noticeable that the outcoupling structures to the right of the main channel appear brighter than the ones to the left, presumably originating from light that is forward-scattered at the aimed outcoupling structure in direction of the following outcoupling sites. Figure 9 shows the results for all channels in comparison by sequentially activating each laser emitter of the diode. The intensity profile shows a significant peak at the outcoupling structure related to the activated laser, reinforcing the finding that specific coupling is possible for all eight channels. The total intensities differ between the channels; for example, waveguide 1 shows only about 35% of the maximum intensity measured at the outcoupling structure of waveguide 3. This disparity is caused, at least partially, by waveguide losses. Due to the different lengths and bending radii of each waveguide from the coupling facet to outcoupling structure, losses differ between the waveguides. Thus, similar coupling into the different waveguides results in unequal intensities at the outcoupling
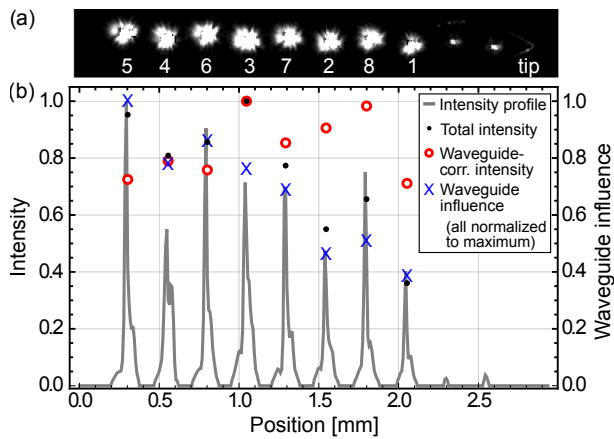
Fig. 9. (a) Outcoupling structure of the waveguide array with all eight lasers of the multibeam diode turned on concurrently, numbered according to Fig. 3; (b) measured intensity profile (line) and the respective total intensities (points) of outcoupling structures for all lasers turned on, and corrected intensity values for each waveguide (circles), corrected for the waveguide influence (crosses, see Table 2).

Table 2.   Waveguide Influence[a]

Waveguide Number	1	2	3	4	5	6	7	8
Relative intensity	0.38	0.46	0.76	0.78	1.00	0.86	0.69	0.51

[a]Relative intensities at the outcoupling structures of the eight waveguides in use based on waveguide losses.

structure. To determine the influence of the waveguides, the respective waveguides were individually characterized in a system with only one laser emitter out of the laser array and each waveguide sequentially adjusted to an ideal coupling position with the laser emitter facet and waveguide aligned on the lenses' optical axis. Table 2 lists the waveguide influence as relative outcoupling intensities for all channels of the probe used for this measurement. These values are used to determine the relation of coupling efficiencies based on the measured total intensities at the outcoupling structure. The relative outcoupling intensities of the sequentially measured waveguides are depicted in Fig. 9 in blue. The simultaneously measured intensities (gray curve, black dots) are corrected with the waveguide-dependent factor, and the corrected values are depicted in red. The corrected values indicate coupling efficiencies of over 70% relative to the maximum coupling efficiency. The still differing values in between the channels can be a sign for non-uniform coupling, but might also originate from variations in the outcoupling structure textures, resulting in non-uniform propagation of stray light toward the sensor.

C. Crosstalk

As suggested before, there is crosstalk between the active channel waveguide and surrounding waveguides, partially as a result of forward-scattered light at the outcoupling structures, but it is also induced while coupling into the waveguide facets and due to losses within each waveguide. Figure 10 shows the crosstalk for each active channel, measured at the outcoupling structure
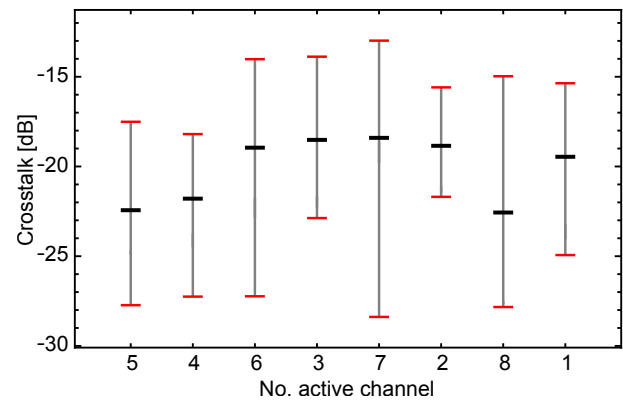
Fig. 10. Crosstalk between active channel and surrounding waveguides/outcoupling structures, displayed for each channel activated sequentially; black lines (bold), mean; red lines, maximum/minimum; numbering of channels according to Fig. 3.

with each channel activated separately. This crosstalk evaluation includes the outcoupling structures of all 10 waveguides, not just the eight active channels. The overall maximum and minimum values for crosstalk are −13.0 dB and −28.4 dB, respectively, with a mean of −20.2 dB.

5. CONCLUSION

A coupling module for the multichannel laser to waveguide array coupling was developed and tested. Simulations as well as experimental results show that a single double-aspheric lens is sufficient to achieve efficient coupling as it reduces spherical aberration and field curvature to a degree that facilitates coupling for eight channels with 100 µm lateral pitch at the incoupling waveguide facets, while maintaining a low crosstalk of less than −13 dB over all channels and outcoupling structures. The results are consistent with those initially measured with a single laser diode. The aspheric lens also allows a high NA necessary for laser diode coupling. Flexible polymer waveguide arrays with lateral channel pitch and longitudinal distance of 25 µm and 250 µm, respectively, at the outcoupling structure were employed as application of the coupling module. The described coupling system can achieve quasi-uniform multichannel coupling, when compared to the degree of variation of other effects inside the cochlea. Light transport from the outcoupling structure of the waveguides through the tissue including bone and light-sensitivity of auditory neurons are expected to be rather non-uniform. The human optical cochlear implant will require certainly channel-dependent adjustments as is the case for the established electrical cochlear implant.

The system could be expanded to 16 channels since the waveguide pitch is met also for laser positions with higher offset than in the recent system. Nevertheless, the coupling efficiency would decrease significantly for channels with higher offset to the optical axis. Thus, coupling systems should be considered also, which allow for an equally distributed optical quality of the individual channels.

Table 3.   Lens 355440: Surface Parameters

R	$+/- 3.200655$ mm
k	-4.321649
A_2	0.0
A_4	$+/- 5.521153\text{E} - 3$
A_6	$-/+ 1.981378\text{E} - 3$
A_8	$+/- 4.782553\text{E} - 4$
A_{10}	$-/+ 7.328134\text{E} - 5$
A_{12}	$+/- 5.920460\text{E} - 6$
A_{14}	$-/+ .104334\text{E} - 8$
A_{16}	$-/+ 1.291935\text{E} - 8$

Table 4.   Lens 355440: Design Parameters

Design wavelength	980 nm
Working Distance	2.7/7.1 mm
Clear Aperture	3.76/4.12 mm
Thickness	3.827 mm
Numeric aperture	0.5/0.3
Effective focal length	2.8 mm
Material	D-ZLAF52LA

APPENDIX A: ASPHERIC LENS PARAMETERS

The surface and design parameters of the double-aspheric lens 355440 listed in Tables 3 and 4 are taken from the respective data sheet [28].

APPENDIX B. OPTICAL CALCULATIONS

The intention of the following calculations is to determine the focus position, as well as the focus spot size, for laser beams propagated through the aspheric lens and the coupling efficiency at the waveguide facet based on geometrical optics.

B1. RAY TRACING

The simulation of the propagation of light through the lens for all laser positions is carried out using ray tracing. Since our lasers operate with divergence angles outside the range for paraxial optics, which requires small-angle approximation, the respective considerations and calculations are insufficient. Thus, we use a geometrically exact approach based on vector analysis. As shown in Fig. 11, every ray consists of n segments as it intersects $n - 1$ surfaces, where each segment can be described with

$$\vec{r}_n = \vec{p}_n + a\vec{b}_n. \tag{B1}$$

For the start, $\vec{p}_1$ is the position vector for the starting point $P_1[0|y_{\text{laser}}| - \text{WD}]$ and

$$\vec{b}_1 = \begin{pmatrix} \tan \phi_x \\ \tan \phi_y \\ 1 \end{pmatrix}, \tag{B2}$$

the starting direction, with WD being the working distance from laser to lens apex, y_{laser} being the slow axis position of the laser, and $\phi_{x/y}$ being the off-axis angles in direction of x and y axis for this specific ray within the beam. The aspheric surface
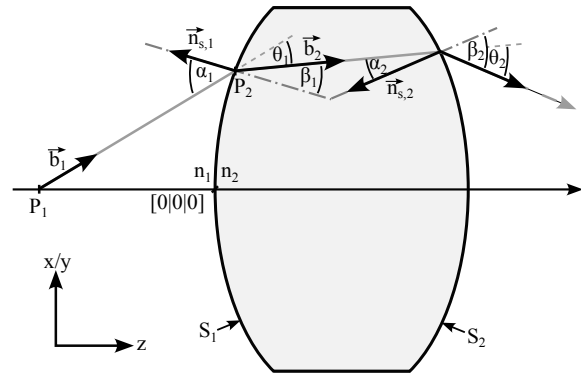
Fig. 11.   Schematic of a single ray propagating through a lens of arbitrary shape.

equation for the nth intersected lens surface is

$$S_n(x, y) = z_{v,n} - \left(\frac{x^2 + y^2}{R_n \left(1 + \sqrt{1 - (k_n + 1)\frac{x^2 + y^2}{R_n^2}} \right)} \right.$$
$$\left. + \sum_{i=2}^{m} A_{2i} \sqrt{x^2 + y^2}^{2i} \right), \tag{B3}$$

with R being the radius of curvature, k being the conic constant, A_{2i} being several aspheric coefficients, and z_v being the vertex position at the optical axis (with $z_{v,1} = 0$). Ray r_n and surface S_n intersect at $P_{n+1}[x_i|y_i|S_n(x_i, y_i)]$, with an incidence angle of

$$\alpha_n = \arccos \left(\frac{-\vec{b}_n \cdot \vec{n}_{s,n}}{|\vec{b}_n||\vec{n}_{s,n}|} \right), \tag{B4}$$

with $\vec{n}_{s,n}$ the lenses surface normal at P_{n+1},

$$\vec{n}_{s,n} = \begin{pmatrix} \frac{dS_n(x_i, y_i)}{dx} \\ \frac{dS_n(x_i, y_i)}{dy} \\ -1 \end{pmatrix}. \tag{B5}$$

The ray is then refracted according to Snell's law, resulting in an emergent angle β_n. The ray section $\vec{r}_{n+1}$ emerging out of this follows Eq. (B1) with

$$\vec{b}_{n+1} = R(\theta_n)\vec{b}_n, \tag{B6}$$

with $R(\theta_n)$ being the rotation matrix [29] to rotate $\vec{b}_n$ around the rotation axis,

$$\vec{n}_R = \vec{n}_{s,n} \times \vec{b}_n, \tag{B7}$$

by an angle of

$$\theta_n = \alpha_n - \beta_n. \tag{B8}$$

B2. FOCAL POINT ANALYSIS

The position and size of the focal points are the main aspects for evaluating the system performance. With a laser as the light source, we can assume a Gaussian beam with normal distribution for the intensity. The laser intensity distribution

$$I(r, \sigma) = \frac{1}{\sqrt{2\pi\sigma^2}} e^{-\frac{r^2}{2\sigma^2}} \quad \textbf{(B9)}$$

depends on the standard deviation σ. Calculating the standard deviation is the basis for determining the focus spot size within the simulated and measured beams. The focus is expected to be the intensity distribution with minimal standard deviation. Since in our system the beam diameter is a directional property, due to astigmatism, the basic equation

$$\sigma^2 = \sum_{i=1}^{n} p_i(x_i - \mu)^2, \quad \textbf{(B10)}$$

with p_i the probability for value x_i to occur, is expanded to

$$\sigma_x^2 = \sum_{i=1}^{n} \frac{I(x_i, y_i)}{I_0}(x_i - \mu_x)^2 | \sigma_y^2 = \sum_{i=1}^{n} \frac{I(x_i, y_i)}{I_0}(y_i - \mu_y)^2,$$
$$\textbf{(B11)}$$

with $I(x_i, y_i)$ being the position dependent intensity value and I_0 being the total intensity and the expected values,

$$\mu_x = \sum_{i=1}^{n} \frac{I(x_i, y_i)}{I_0} x_i | \mu_y = \sum_{i=1}^{n} \frac{I(x_i, y_i)}{I_0} y_i. \quad \textbf{(B12)}$$

In the measured beam profiles, $I(x_i, y_i)$ equals the brightness value for each camera sensor pixel. For the ray traced beam, every ray represents the same intensity. Thus, the piercing points of each ray through the series of evaluated planes determine the standard deviation. The coupling efficiency is then calculated as the ratio of rays piercing through the focal plane within a specified waveguide facet area to the total number of rays.

Disclosures. C. G., D. K., T. M., and U. S. are cofounders of the OptoGenTech Company.

Data availability. Data underlying the results presented in this paper are not publicly available at this time but may be obtained from the authors upon reasonable request.

REFERENCES

1. T. Moser, "Optogenetic stimulation of the auditory pathway for research and future prosthetics," Curr. Opin. Neurobiol. **34**, 29–36 (2015).
2. A. Dieter, D. Keppeler, and T. Moser, "Towards the optical cochlear implant: optogenetic approaches for hearing restoration," EMBO Mol. Med. **12**, e11618 (2020).
3. V. H. Hernandez, A. Gehrt, K. Reuter, *et al.*, "Optogenetic stimulation of the auditory pathway," J. Clin. Invest. **124**, 1114–1129 (2014).
4. D. Keppeler, C. A. Kampshoff, A. Thirumalai, *et al.*, "Multiscale photonic imaging of the native and implanted cochlea," Proc. Natl. Acad. Sci. USA **118**, e2014472118 (2021).
5. S. Balster, G. I. Wenzel, A. Warnecke, *et al.*, "Optical cochlear implant: evaluation of insertion forces of optical fibres in a cochlear model and of traumata in human temporal bones," Biomed. Eng. **59**, 19–28 (2014).
6. D. Miyamoto and M. Murayama, "The fiber-optic imaging and manipulation of neural activity during animal behavior," Neurosci. Res. **103**, 1–9 (2016).
7. A. Klimas and E. Entcheva, "Toward microendoscopy-inspired cardiac optogenetics in vivo: technical overview and perspective," J. Biomed. Opt. **19**, 080701 (2014).
8. Y. Zhao, H. Nakamura, and R. J. Gordon, "Development of a versatile two-photon endoscope for biological imaging," Biomed. Opt. Express **1**, 1159–1172 (2010).
9. H. D. Park, H.-J. Shin, I.-J. Cho, *et al.*, "The first neural probe integrated with light source (blue laser diode) for optical stimulation and electrical recording," in *Annual International Conference of the IEEE Engineering in Medicine and Biology Society* (2011), pp. 2961–2964.
10. K. Kwon and W. Li, "Integrated multi-led array with three-dimensional polymer waveguide for optogenetics," in *IEEE 26th International Conference on Micro Electro Mechanical Systems (MEMS)* (2013), pp. 1017–1020.
11. A. N. Zorzos, E. S. Boyden, and C. G. Fonstad, "Multiwaveguide implantable probe for light delivery to sets of distributed brain targets," Opt. Lett. **35**, 4133–4135 (2010).
12. A. N. Zorzos, J. Scholvin, E. S. Boyden, *et al.*, "Three-dimensional multiwaveguide probe array for light delivery to distributed brain circuits," Opt. Lett. **37**, 4841–4843 (2012).
13. P. Karioja and D. Howe, "Diode-laser-to-waveguide butt coupling," Appl. Opt. **35**, 404–416 (1996).
14. Y. M. Cheung and C. H. Yiu, "Simulation of the alignment sensitivity on the coupling efficiency of a ball-lens capped to-can laser diode source into a single-mode fiber," in *4th International Symposium on Electronic Materials and Packaging* (IEEE, 2002).
15. P.-I. Dietrich, M. Blaicher, I. Reuter, *et al.*, "In situ 3D nanoprinting of free-form coupling elements for hybrid photonic integration," Nat. Photonics **12**, 241–247 (2018).
16. C. A. Edwards, H. M. Presby, and C. Dragone, "Ideal microlenses for laser to fiber coupling," J. Lightwave Technol. **11**, 252–257 (1993).
17. Y. Tottori, T. Kobayashi, and M. Watanabe, "Low loss optical connection module for seven-core multicore fiber and seven single-mode fibers," IEEE Photon. Technol. Lett. **24**, 1926–1928 (2012).
18. K. Shiraishi, N. Oyama, K. Matsumura, *et al.*, "A fiber lens with a long working distance for integrated coupling between laser diodes and single-mode fibers," J. Lightwave Technol. **13**, 1736–1744 (1995).
19. D. Zhou and E. Greenbaum, eds., *Implantable Neural Prostheses 2* (Springer, 2010).
20. H. Zhou, H. Xu, and J. Duan, "Review of the technology of a single mode fiber coupling to a laser diode," Opt. Fiber Technol. **55**, 102097 (2020).
21. T. Kato, F. Yuuki, K. Tanaka, *et al.*, "A new assembly architecture for multichannel single mode-fiber-pigtail LD/PD modules," IEEE Trans. Compon. Hybrids Manuf. Technol. **16**, 89–94 (1993).
22. S.-M. Yeh, Y.-K. Lu, S.-Y. Huang, *et al.*, "A novel scheme of lensed fiber employing a quadrangular-pyramid-shaped fiber endface for coupling between high-power laser diodes and single-mode fibers," J. Lightwave Technol. **22**, 1374–1379 (2004).
23. K. Kampasi, D. F. English, J. Seymour, *et al.*, "Dual color optogenetic control of neural populations using low-noise, multishank optoelectrodes," Microsyst. Nanoeng. **4**, 10 (2018).
24. L. Rudmann, S. D. Huber, J. S. Ordonez, *et al.*, "Fused silica microlenses for hermetic packages as part of implantable optrodes," in *37th Annual International Conference of the IEEE Engineering in Medicine and Biology Society (EMBC)* (2015), pp. 7143–7146.
25. J. Alda, D. Vazquez, and E. Bernabeu, "Wavefront and amplitude profile for astigmatic beams in semiconductor lasers: analytical and graphical treatment," J. Opt. **19**, 201–206 (1988).
26. G. Romanova, T. Ivanova, T. Zhukova, *et al.*, "Influence of aspherical surfaces description on aberration correction," Proc. SPIE **9626**, 757–763 (2015).
27. C. Helke, M. Reinhardt, M. Arnold, *et al.*, "On the fabrication and characterization of polymer-based waveguide probes for use in future optical cochlear implants," Materials **16**, 106 (2023).
28. LightPath Technologies, "Lens code 355440, 0355440 data sheet," 2015, https://www.lightpath.com/wp-content/uploads/2021/08/0355440.pdf.
29. E. Kovács, "Rotation about an arbitrary axis and reflection through an arbitrary plane," Ann. Math. Inf. **40**, 175–186 (2012).